ASME Journal of Manufacturing Science and Engineering
Online journal at:
https://asmedigitalcollection.asme.org/manufacturingscience

Kuan Lu
J. Mike Walker '66 Department of Mechanical Engineering,
Texas A&M University,
3123 TAMU,
College Station, TX 77843-3123
e-mail: lukuan@tamu.edu

Zhikun Wang
L&T Technology Services (Vendor for Meta Platforms),
9845 Willows Road Northeast,
Redmond, WA 98052
e-mail: wangzhikun@tamu.edu

Heebum Chun
J. Mike Walker '66 Department of Mechanical Engineering,
Texas A&M University,
3123 TAMU,
College Station, TX 77843-3123
e-mail: chun@tamu.edu

ChaBum Lee[1]
J. Mike Walker '66 Department of Mechanical Engineering,
Texas A&M University,
3123 TAMU,
College Station, TX 77843-3123
e-mail: cblee@tamu.edu

Wafer Edge Metrology and Inspection Technique Using Curved-Edge Diffractive Fringe Pattern Analysis

This paper introduces a novel wafer-edge quality inspection method based on analysis of curved-edge diffractive fringe patterns, which occur when light is incident and diffracts around the wafer edge. The proposed method aims to identify various defect modes at the wafer edges, including particles, chipping, scratches, thin-film deposition, and hybrid defect cases. The diffraction patterns formed behind the wafer edge are influenced by various factors, including the edge geometry, topography, and the presence of defects. In this study, edge diffractive fringe patterns were obtained from two approaches: (1) a single photodiode collected curved-edge interferometric fringe patterns by scanning the wafer edge and (2) an imaging device coupled with an objective lens captured the fringe image. The first approach allowed the wafer apex characterization, while the second approach enabled simultaneous localization and characterization of wafer quality along two bevels and apex directions. The collected fringe patterns were analyzed by both statistical feature extraction and wavelet transform; corresponding features were also evaluated through logarithm approximation. In sum, both proposed wafer-edge inspection methods can effectively characterize various wafer-edge defect modes. Their potential lies in their applicability to online wafer metrology and inspection applications, thereby contributing to the advancement of wafer manufacturing processes. [DOI: 10.1115/1.4065639]

Keywords: wafer metrology and inspection, interferometry, fringe pattern, diffraction, pattern analysis, semiconductor manufacturing, sensors

1 Introduction

The continuously growing demand in the semiconductor device market for high performance, low energy consumption, high reliability, and low cost has driven the need for decreased critical dimension (CD) and high-volume manufacturing [1]. With 400–1200 manufacturing processes involved in producing a semiconductor chip, it becomes challenging to implement comprehensive controls across the entire manufacturing process. Due to ever-decreasing CD features in the device patterns, the importance of wafer defect inspection becomes paramount.

Wafer metrology and inspection are crucial components of semiconductor manufacturing processes, playing a vital role in maintaining high wafer quality and facilitating root cause analysis [2,3]. These systems detect physical and pattern defects on wafers, providing precise defects' location and classification information with high sensitivity and throughput. They contribute to improved yield, collect comprehensive data for advancing manufacturing processes, and are instrumental in defect prevention, process optimization, and semiconductor production efficiency enchantment.

Wafer-edge inspection holds significant importance among inspections as it addresses various defects that are prone to occur in the critical region spanning from the upper near edge zone to the bottom near edge zone. These defects include particles, scratches, thin-film deposition, and chipping. Studies have shown that the yield rate at the wafer edge is significantly lower, amounting to only 50% of that at the center under certain circumstances [4]. Nevertheless, implementing effective wafer-edge inspection can substantially enhance the overall yield, potentially increasing it by up to 10% [5]. Additionally, edge inspection is vital to identify the underlying causes of edge defects, providing insights into process variations or issues. This information allows manufacturers to take targeted corrective actions, optimize their processes, and maintain consistent wafer quality [6]. To meet these requirements, there is a growing demand for advanced wafer-edge inspection tools capable of not only detecting defects but also quantifying them while profiling the wafer geometry. These tools enable precise monitoring and control of wafer-edge quality, thereby contributing to the production of high-quality semiconductor devices.

Top players in the semiconductor metrology and inspection industry (KLA Corporation, Applied Materials, Hitachi High-Technologies, JEOL, and ASML) have introduced a range of optical inspection tools based on bright-field, dark-field, or combined optical microscopy techniques [7]. However, such inspection systems are extremely expensive and remain a challenge to achieve

[1]Corresponding author.
Manuscript received June 12, 2023; final manuscript received March 10, 2024; published online June 10, 2024. Assoc. Editor: Gregory Vogl.

extremely high resolution, aiming at one-twentieth of the light wavelength [8–10]. In recent years, artificial intelligence (AI) technology such as deep learning has been widely adopted not only in wafer inspection but also in the overall semiconductor design and manufacturing processes. AI provides an innovative and effective solution to overcome the critical challenges in wafer defect inspection, but it is still limited to identifying and classifying the wafer defects [11–13].

In the studies regarding wafer inspection, high-resolution microscopy, such as atomic force microscopy (AFM), transmission electron microscopy (TEM), and scanning electron microscopy (SEM), is widely adopted in the industry [14–19]. Equipped with powerful image processing algorithms, these systems can visualize the various defects with CD feature size down to 1 nanometer, even to the sub-nanometer scale. However, their inspection speed is slow and sometimes requires a high vacuum environment condition that those tools are adapted as post-process inspection methods although the industry wants to do online or inline wafer inspection to increase productivity.

Lee and coauthors introduced knife-edge interferometry (KEI) for displacement measurement [20–23], cutting tool edge quality inspection [24–26], and photomask line width and line-edge-roughness characterization [27,28]; he also applied curved-edge interferometry to in-process spindle health and dynamic behavior monitoring [29,30].

Inspired by the applications of KEI, curved-edge interferometry (CEI) was further introduced in this study to be utilized for wafer-edge metrology and inspection. Different from KEI, which uses an ideal non-thickness edge, curved-edge was considered as the boundary between the incident wave and measurement waves, the measured waves further overlap and produce interference fringes. While CEI is more complicated since asymptotic solutions to few canonical problems related to edge topological conditions are required, diffractive patterns of CEI also convey more useful information and could be extracted through statistical feature extraction and wavelet transform methods. In this study, two setups were developed: the single-point scanning setup, evolved from KEI experiment, is capable of wafer apex characterization, but the areal imaging setup features high efficiency and enables simultaneous characterization of wafer-edge quality along two bevels and apex directions. Details of wafer-edge inspection and fringe pattern analysis methods will be explained, and prospective applications and future enhancements of the proposed methods are discussed.

2 Measurement Principle

In this study, CEI was adapted for wafer-edge metrology and inspection. When the incident light interacts with any type of edges (e.g., sharp, circular, or any free-form shape), a diffractive fringe pattern, the so-called interferogram, is created in the observation plane due to the interference of two superimposing waves, which are the transmitted wave from the incident light source and the diffracted wave from the secondary source. The diffractive fringe patterns in the observation plane have demonstrated different characteristics according to the edge geometrical conditions. The amplitude, frequency, and phase of diffractive fringe patterns can be changed in accordance with the edge shape, size, and roughness. Thus, the diffractive fringe patterns can be expected as a result of the total field in the observation plane that is derived by using the inverse Fourier transform [28,32,33].

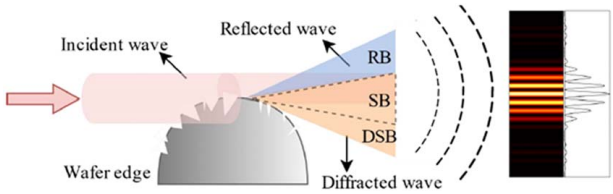

Fig. 1 Schematic principle of curved-edge diffraction

The physical models of knife-edge diffraction have been introduced in many studies [19–23,25–27,30,31]. Unlike knife-edge diffraction, the diffraction effect that takes place in a curved edge is complex because curved-edge diffraction introduces three boundaries (reflection, shadow, and deep shadow) and requires the asymptotic solution to several canonical problems associated with the edge shape and topological conditions. As shown in Fig. 1, three different waves are generated when an electromagnetic wave propagates to the shadow boundary of a curved edge, including an incident wave, a reflected wave, and an edge-diffracted wave. These waves further interact and create three different regions, which are the reflection boundary (RB), shadow boundary (SB), and deep shadow boundary (DSB). The fringe data can be obtained in these regions.

Curved-edge interferometry is a suitable method for edge defect detection [29,30], since diffraction patterns formed in those regions are significantly influenced by the edge geometry, topography, and contaminants. Therefore, profound information about the edge quality can be extracted through the analysis of the collected fringe data.

3 Experiments

3.1 Experiments Setup. In this study, a total of seven wafer-edge cases were evaluated. The reference case represented a wafer edge with no defects, serving as a control group for comparison. Various defect modes were artificially added to the other wafer edges, including four single-mode cases (scratched, chipped, particle contamination, and film deposition) and two combined mode cases (chipped with particles and chipped with thin film). By evaluating these different wafer-edge cases, the study aimed to assess the performance of the proposed wafer-edge inspection methods and their ability to detect and characterize various defect modes.

Two experiment setups were developed, a green laser ($\lambda =$ 532 nm) and a blue laser ($\lambda = 473$ nm) were employed as laser sources, respectively. Figure 2(*a*) describes the experimental setup for obtaining fringe patterns. The sample wafer was securely fixed on a precision linear stage. The laser first propagated through an aperture (ϕ1.0 mm), interacted with the wafer edge, and shined on the avalanche photodiode (APD) sensor. While the wafer

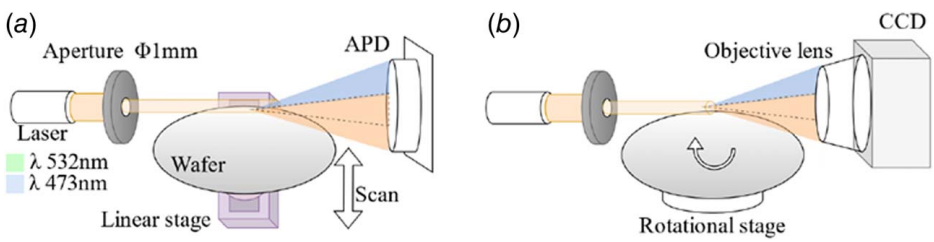

Fig. 2 Schematics of Experiment setup: (*a*) single-point scanning method and (*b*) areal imaging method

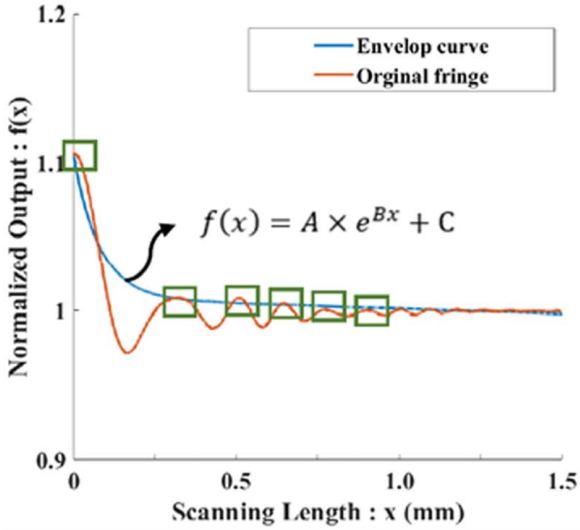

Fig. 3 Logarithm approximation demonstration

moved at a constant speed of 1 mm/s, the output voltage of APD was collected by a data acquisition device. Figure 2(*b*) depicts the setup to acquire the diffraction pattern images. The sample wafer was fixed on a rotational stage, and a charge-coupled device (CCD) was positioned at the end to capture the image. A 20× objective lens was coupled with CCD, to enhance the image quality and resolution.

Different from the mechanical scanning in the first setup, the wafer scanning in the areal imaging method was achieved by extracting fringe patterns at specific directions and distances in the images. Both methods can effectively analyze the fringes, allowing for the extraction of information on the wafer edge, which can be further utilized for quantifying and analyzing the edge defect features.

3.2 Data Analysis Methods. For the single-point scanning method, fringe curves along the apex were directly obtained from the APD sensor. For the areal imaging method, diffraction images were captured and used to extract fringe intensity distribution spectrograms along three directions: apex, lower bevel, and upper bevel. Appropriate filters were applied to remove DC signals and noise, ensuring that only relevant fringe information was retained.

Fringe curves of different defect cases were individually compared with the reference to calculate the cross-correlation value, which quantitatively represents the similarity between two fringes. The cross-correlation coefficient is obtained by dividing the covariance of two variables by their respective standard deviation:

$$r = \frac{\sum_{i=1}^{n}(X_i - \bar{X})(Y_i - \bar{Y})}{\sqrt{\sum_{i=1}^{n}(X_i - \bar{X})^2}\sqrt{\sum_{i=1}^{n}(Y_i - \bar{Y})^2}} \tag{1}$$

The cross-correlation value r ranges from −1 to 1 and when two groups of data become identical, the value comes to 1.

The fitted parameters of logarithm approximation also serve as extracted features [34]. Figure 3 demostrates the process of curve fitting through approximation. Considering the fast fringe intensity decay rate of higher orders, an exponential function was chosen for the envelope curve. In the envelope curve f, x is the scanning length, A and B are parameters to be fitted, which are considered as extracted features of edge quality, and C is a constant term.

Wavelet analysis is a well-established signal processing technique and was adapted to extract and analyze the features of different fringes [27]. In the single-point scanning method, defect cases were categorized into two groups: single defects and hybrid defects. For each group, all defective fringe curves, along with reference fringe, were collectively analyzed using the wavelet feature extraction method. Corresponding wavelet indexes, which quantitatively assessed the severity of the defects, were further obtained. In the case of the areal imaging method, continuous wavelet transform (CWT) was directly applied to each extracted fringe intensity curve. The transformed CWT scalograms visually represent the frequency content of the fringes, providing profound insights into the frequency characteristics.

4 Results

4.1 Single-Point Scanning Method. The fringe distributions are shown in Fig. 4. The cross-correlation values extracted from raw data are presented in Fig. 5. Overall, the following results can be obtained:

(1) All orders of fringes attenuated or even vanished when the defect deteriorates.
(2) A decreased cross-correlation value indicates a larger fringe difference compared to the no-defect case. Statistical feature extraction results intuitively reflect the change in edge quality.

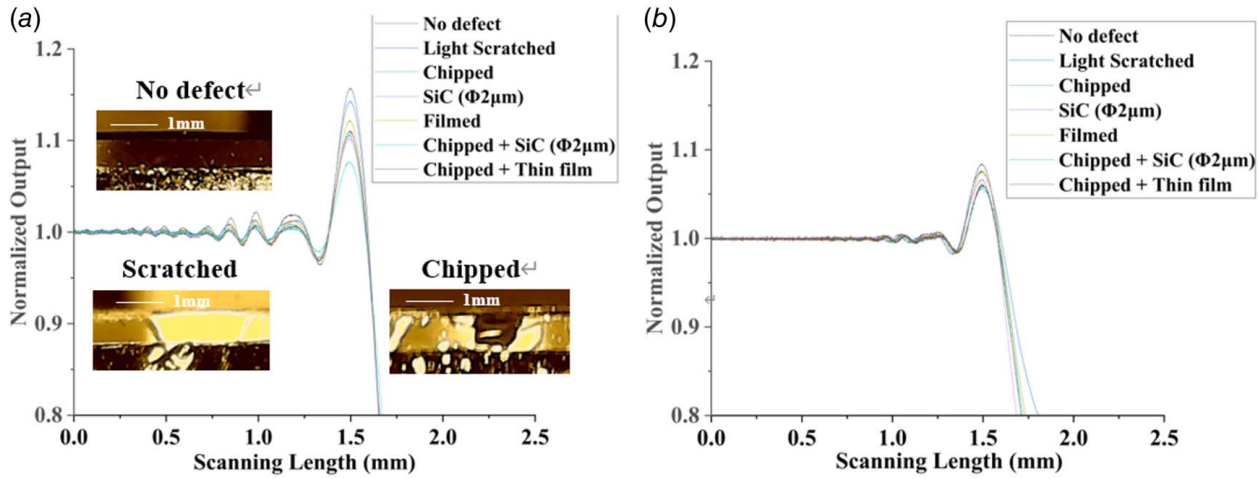

Fig. 4 Interferometric fringe patterns according to the defect modes: (*a*) $\lambda = 532$ nm and (*b*) $\lambda = 473$ nm

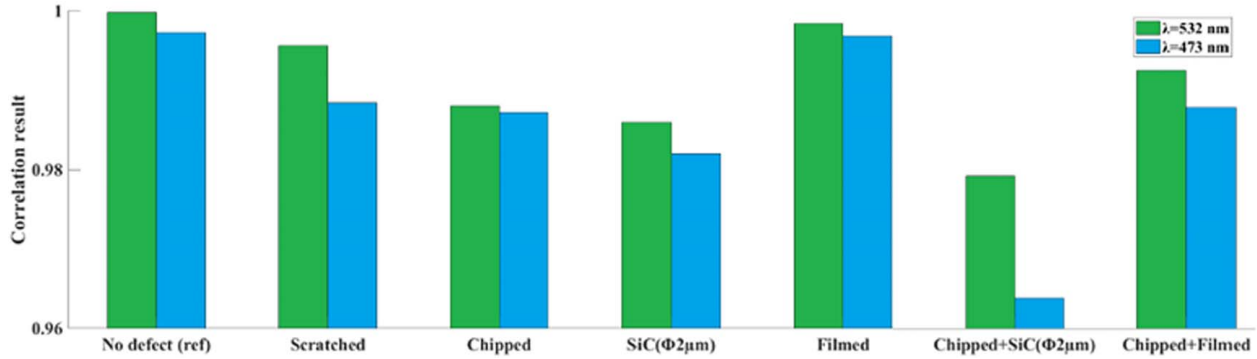

Fig. 5 Cross-correlation values of defect mode analysis results

(3) The results demonstrate a high sensitivity of the proposed method to different defect modes, highlighting its ability to quantitatively characterize edge quality.

Taking the $\lambda = 532$ nm scenario as an example, the intensity of first order in scratched and chipped fringes decreased by 1.21% and 4.47%, respectively. For particle and film cases, fringes intensity of first order dropped from 1.157 to 1.101 and 1.121, respectively, which could be explained by the fact that film deposition usually results in a better surface integrity compared to particles. The fringe data from the combined defect mode showed a more complicated behavior. The presence of particles on the chipped edge further deteriorated the edge quality, leading to an even attenuated fringe pattern and a decreased cross-correlation value, from 0.9880 to 0.9792. Conversely, the thin film on the chipped edge reduced its roughness and had the opposite effect on experimental data: cross-correlation increased to 0.9925. Similar trends were observed in the $\lambda = 473$ nm case. The presence of particles on the chipped edge led to a decrease in the cross-correlation value by 2.37% while adding thin film to the chipped edge slightly increased the fringe similarity to 0.9878 from 0.9872.

From the results in Fig. 6, fringe patterns and their corresponding edge quality characteristic are numerically illustrated by the enveloping curve parameters. As the edge conditions worsen, A and B both show a consistent decreasing tendency. Based on the approximation formula, a smaller A reflects lower fringe peak magnitudes, and a smaller B represents a faster peak attenuation rate. In the single mode case, when $\lambda = 532$ nm, A decreased by 32.65% and B decreased by 37.89% as the edge quality worsened. Similarly, in the $\lambda = 473$ nm case, A decreased by 28.87% and B decreased by 33.84% as the edge quality worsened. Considering the Chipped + SiC ($\Phi 2$ μm) case, when $\lambda = 532$ nm and $\lambda = 473$ nm, A decreased by 49.19% and 25.57%, while B decreased by 51.86% and 38.72% respectively, when compared with the reference. These significant reductions in parameters A and B show a rapid intensity diminution in its fringes, in both peak magnitudes and attenuation rates.

Figure 7 depicts the outcome of wavelet-based feature extraction. By decomposing the raw data across multiple scales using a series of filters, the coefficients obtained from each resultant component serve as the extracted features. These features contain crucial

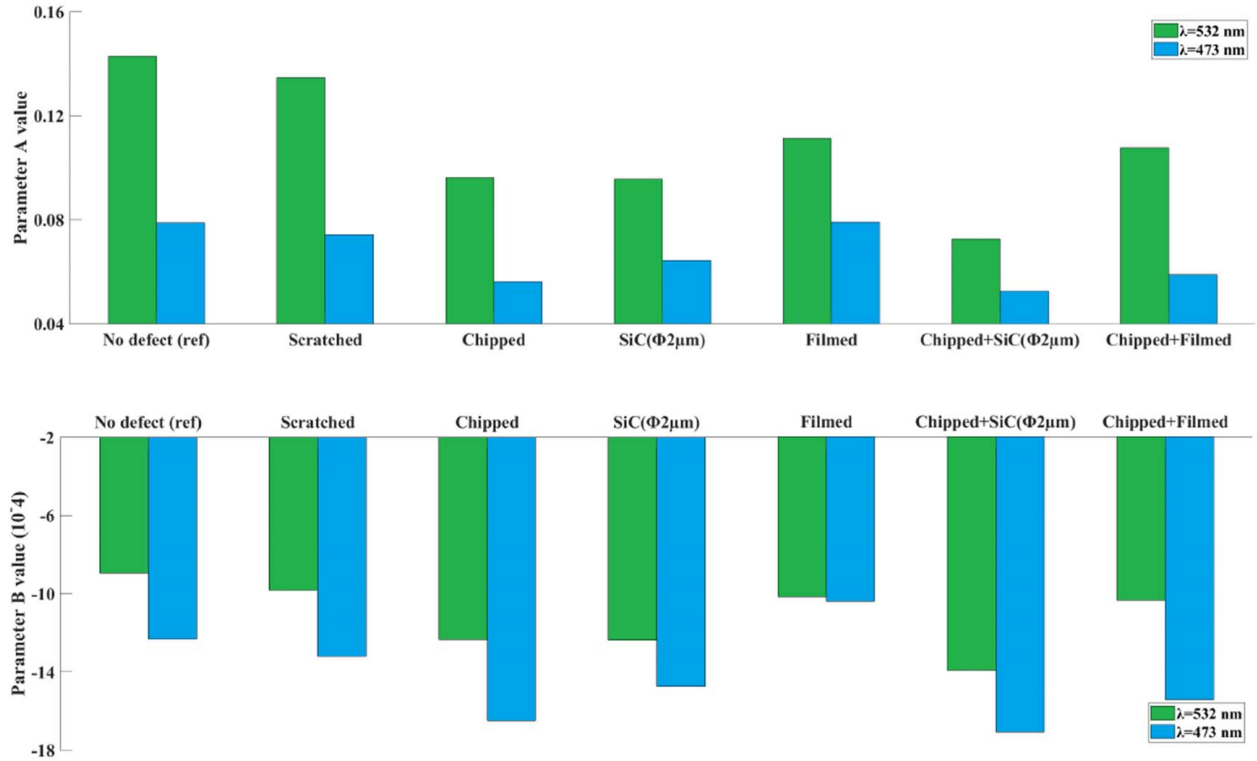

Fig. 6 Fitting results of logarithm approximation

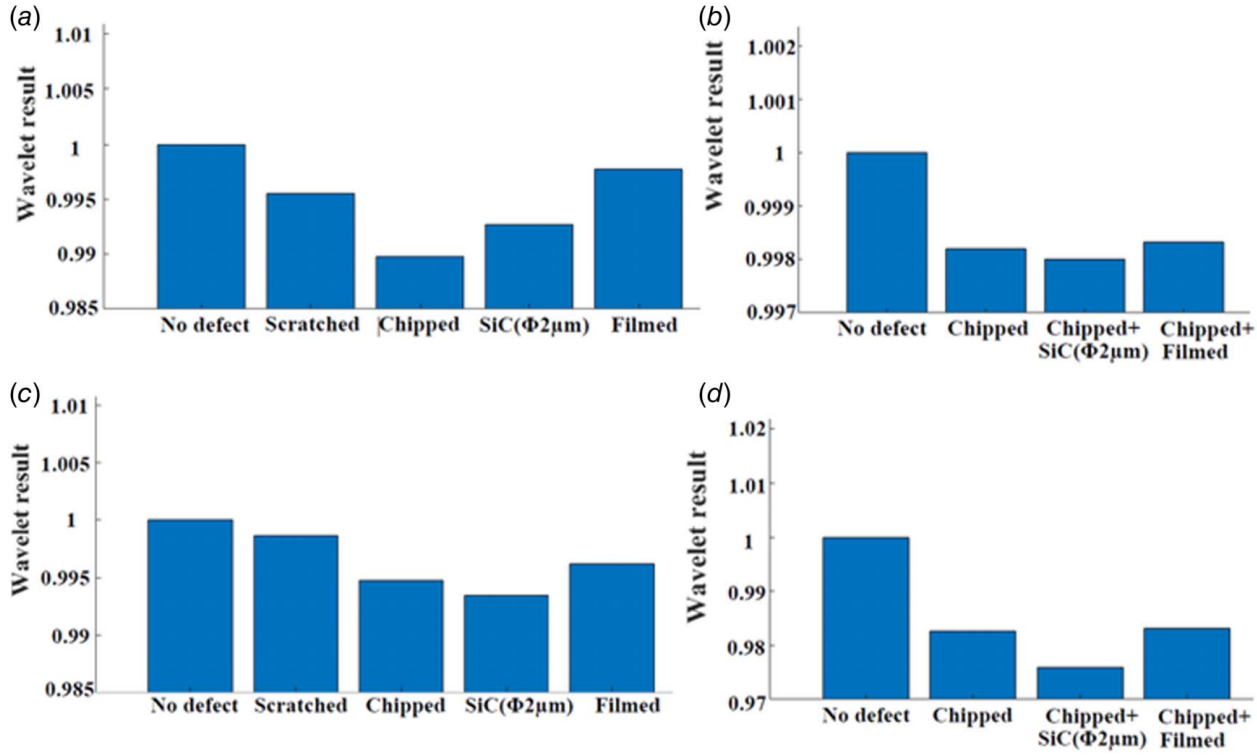

Fig. 7 Wavelet feature results of experiment data (*a*) and (*b*) $\lambda = 473$ nm and (c) and (*d*) $\lambda = 532$ nm

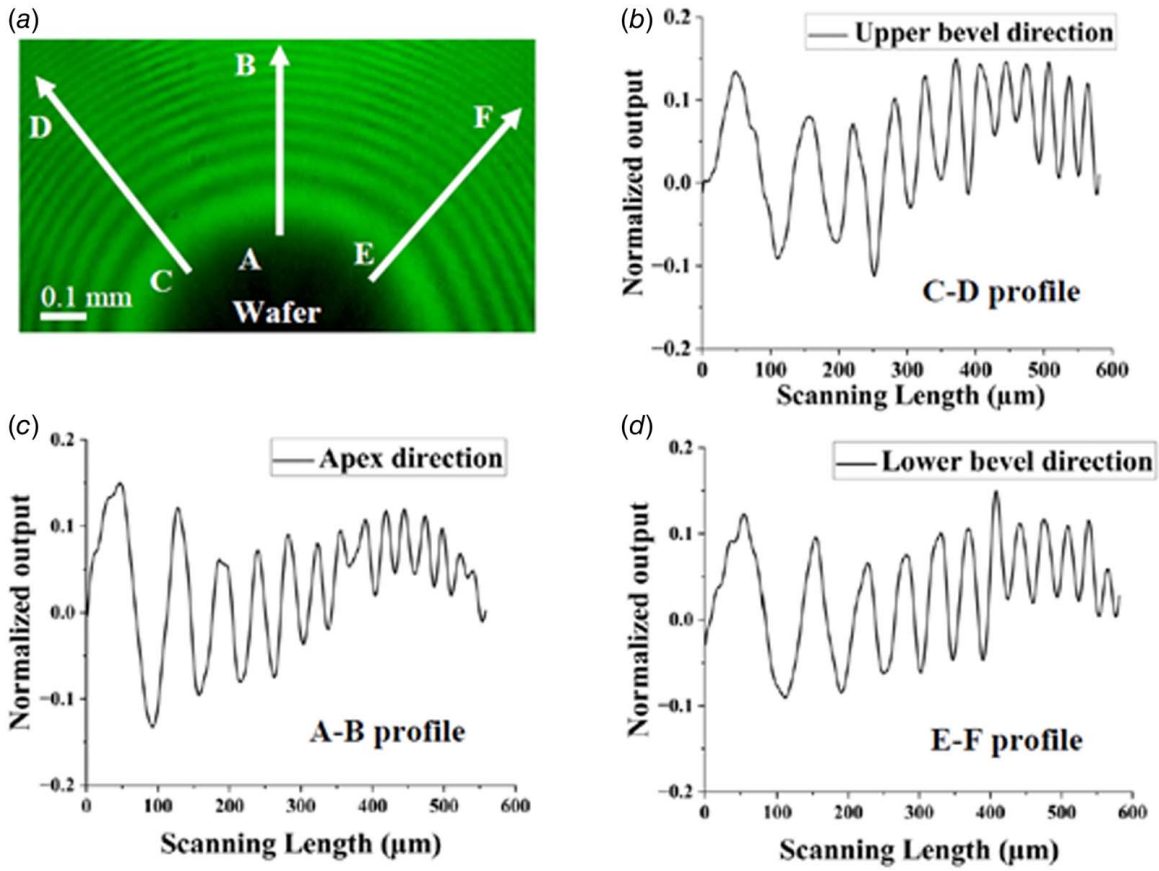

Fig. 8 Demonstration of diffraction images and fringe intensity along apex direction, upper bevel direction, and lower bevel direction: (*a*) interferogram image and fringe pattern profiles along (*b*) the upper bevel, (c) the apex and (*d*) the lower bevel

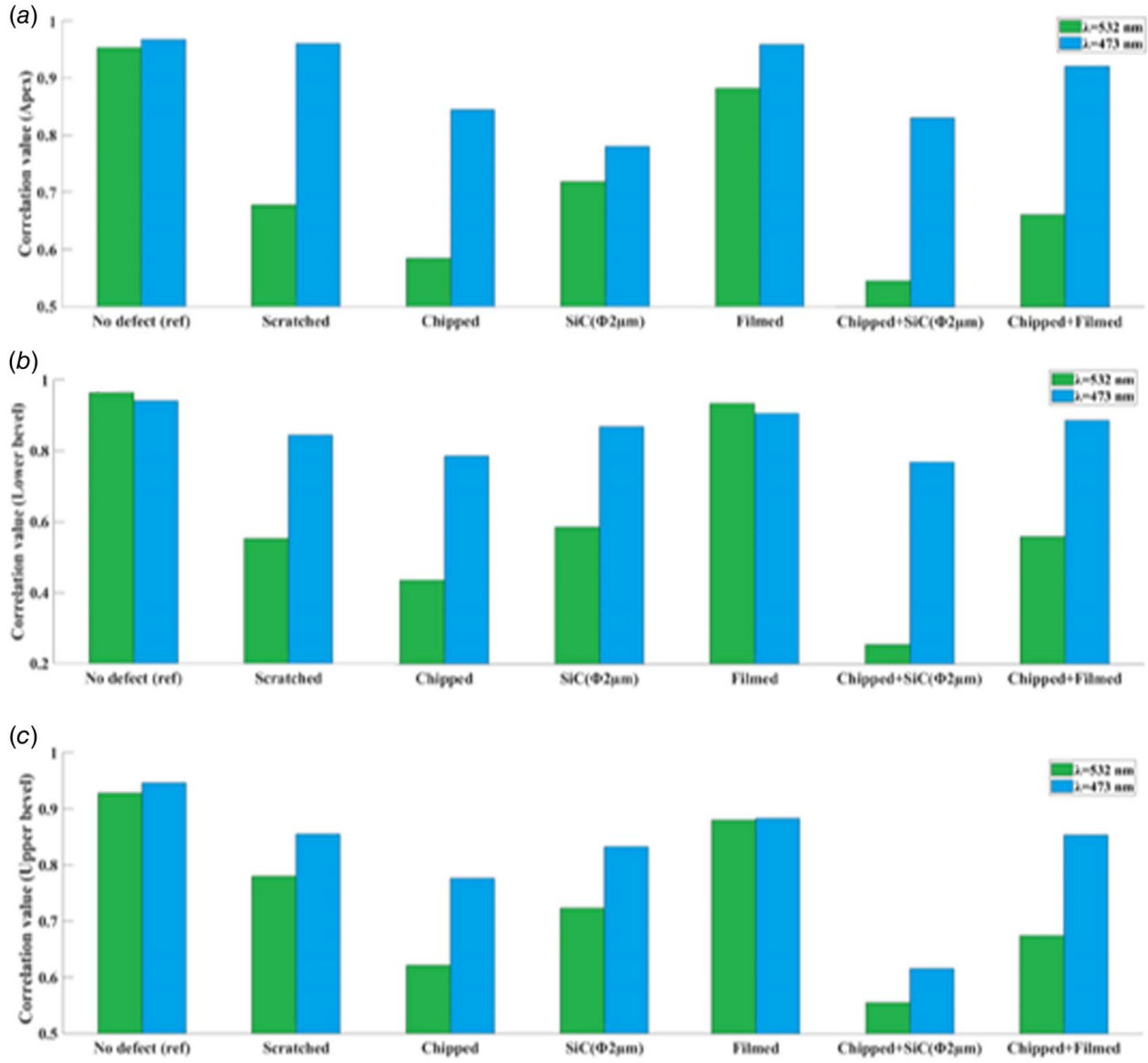

Fig. 9 Cross-correlation values of defect mode analysis results along (*a*) apex direction, (*b*) lower bevel direction, and (*c*) upper bevel direction

time–frequency information inherent to the original fringe data and A feature selection is then conducted to identify the features with the most discrimination ability [27,35,36]. The selected index in Fig. 7 serves as the representation of the defect severity, with a lower index indicating a more severe edge defect and a higher index indicating a less severe edge defect.

In Figs. 7(*a*) and 7(*c*), the chipped case had a smaller index than that of the scratched case, while the filmed case had a larger index than that of the particle contamination case. Furthermore, edge quality in combined defect modes is also reflected by the wavelet index. particle pollutants on the chipped edge further degraded the edge quality, indicated by a lower index, while film deposition improved the chipped edge integrity, resulting in a higher index, as indicated in Figs. 7(*b*) and 7(*d*). The results highlight the effectiveness of the wavelet analysis in distinguishing between different defect modes and assessing the edge quality in various defect scenarios.

4.2 Areal Imaging Method. As described in Sec. 3.2, diffraction patterns were converted into fringe intensity distribution along lower bevel, upper bevel, and apex, which is also demonstrated in Fig. 8. This method is able to simultaneously localize and evaluate defects present in each direction, providing a comprehensive understanding and valuable insights into the defect distribution and overall quality of the wafer edge.

The data processing results are shown in Fig. 9, and the following results can be obtained:

(1) Defects along the lower bevel, upper bevel, and apex can be localized, and their corresponding edge quality can be characterized simultaneously. For instance, under $\lambda = 473$ nm experimental condition, the cross-correlation value decreased by 7.39%, 9.21%, and 12.11% in three directions (lower bevel, upper bevel, and apex) when the defect deteriorated from scratched to chipped. Furthermore, it increased by 9.97%, 12.77%, and 10.09% when film deposition was added to the chipped edge, the result suggests that thin film on the chipped wafer tends to improve edge quality, especially in the upper bevel direction.
(2) Overall, the statistical feature extraction results in all directions are consistent with that of the single-point scanning

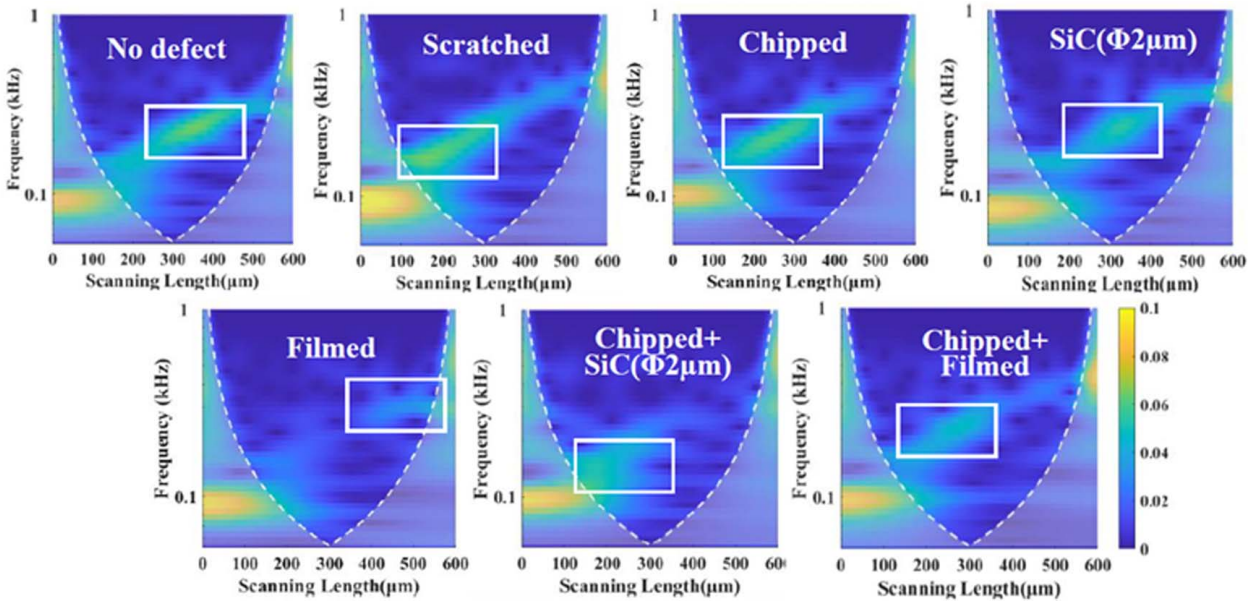

Fig. 10 1D Wavelet transformation scalogram on apex direction (A–B; $\lambda = 532$ nm)

method. As the edge roughness increases, the similarity between the fringe pattern and the no-defect case decreases, leading to a decrease in the cross-correlation value.

(3) The imaging method is highly sensitive to changes in edge topology. Taking the Chipped + SiC ($\phi 2$ μm) case as an example, under $\lambda = 532$ nm condition, the cross-correlation values along the lower and upper bevels are only 0.2542 and 0.5550, respectively. This could be attributed to the accumulation of particles on a roughened chipped surface, forming a complex and irregular topology, causing diffraction patterns to undergo significant changes.

Wavelet analysis is preliminarily introduced to conduct wafer edge feature extraction in this study. Figures 10 and 11 illustrate the wavelet transformation scalogram of the diffraction pattern in the apex direction when two lasers were employed respectively. "Morse" wavelet, a specific complex wavelet utilized for multiresolution analysis, was selected as the mother wavelet in this study to create the scalograms. The y-axis represents the frequency in logarithmic scale, which is calculated by

$$f_{actual} = \frac{\omega_0 \times f_s}{2\pi s} \tag{2}$$

where f_{actual} is the actual frequency derived from wavelet transform, ω_0 is the center frequency of the "Morse" wavelet, f_s is the sampling frequency, and s is the wavelet scale. Different scales capture information about the data at varying frequency bands, with a larger scale indicating a lower frequency.

The wavelet results indicate that fringe patterns of various defect samples exhibit distinct time–frequency domain properties. The

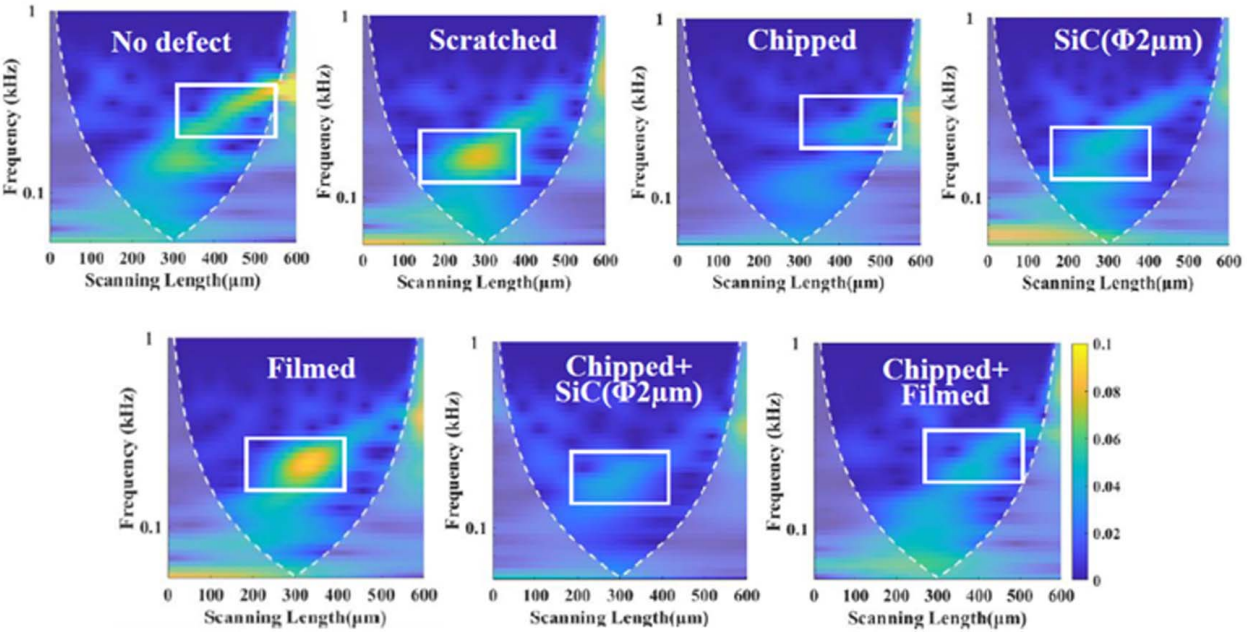

Fig. 11 1D Wavelet transformation scalogram on apex direction (A–B; $\lambda = 473$ nm)

spectral charts are a visual tool to comprehend how different edge conditions influence light propagation and scattering. The no-defect case is the baseline, displaying the spectral response of the edge without defect. It features a pronounced peak intensity region, and the dominant frequency complement showed shifting in tendency and changing the frequency when defects presented.

Defects could elicit a strong response at a specific frequency; take $\lambda = 532$ nm case as an instance, the dominant frequency of no-defect case was observed between 250 and 450 μm at 230 Hz frequency with a magnitude of 0.0647; that of the chipped case was observed between 150 and 350 μm, a 100 μm left shirting, at 206 Hz frequency with a magnitude of 0.0596. The results also show that chipping resonated at another frequency compared with the scratched case. The spectral charts for combined defects depict more complex responses when multiple defects interact. For example, when particles were added to the chipped edge, the location of the dominant frequency further moved left by 50 μm, and its value decreased to 136 Hz with a magnitude of 0.0509.

For a given setup, as the wavelength gets shorter, the spacing between the fringes decreases which results in more fringes being present within a given space, which could contribute to a better differentiation of subtle features and a more efficient capture of intricacies difference. For instance, in combined defects cases like "Chipped + SiC(Φ2 um)" and "Chipped + Filmed," the response appears more dispersed under the $\lambda = 473$ nm laser setup, and a more layered interaction and broader frequency response also indicate that the $\lambda = 473$ nm laser could offer a more comprehensive and detailed perspective into edge defects.

5 Conclusion and Future Works

This paper proposed a new wafer-edge quality inspection technology based on the analysis of curved-edge diffraction fringe patterns, which is featured as both cost-effective and efficient. Two approaches, namely the single-point scanning method and areal imaging method, were developed, and the camera-based imaging system also enabled simultaneous characterization of wafer quality along all directions.

This study thoroughly analyzed various defect cases, including both single and combined modes. The fringe scalogram was characterized through statistical feature extraction methods, wavelet transform, and logarithm approximation. From the results, it was confirmed that edge quality could be reflected by changes in various extracted features from the fringe data, including cross-correlation value, envelop curve parameters, and continuous wavelet analysis. Furthermore, the 1D wavelet transformation showed potential in edge quality detection automation through time–frequency domain properties characterization. Implementing the proposed methods in industry leads to increased wafer production yield, improved throughput, and reduced operational costs, thereby benefiting both the company and the environment in the long term.

For future work, this paper suggests exploring advanced pattern recognition methods or deep learning techniques to enhance real-time and quantitative defect inspection of the wafer edge, as the AI has already been successfully applied in fringe pattern defect identification [37–39]. For instance, by integrating deep learning with the wavelet analysis method, at which frequency bands defect response and how the intensity of response changes could be better understood, which is crucial for automatic defect categorization and characterization, and efficiency and accuracy of the inspection process could be further improved.

Author Contribution Statement

All authors contributed equally to this work.

Acknowledgment

This research has been supported by the National Science Foundation (CMMI #1855473, #212499).

Conflict of Interest

There are no conflicts of interest.

Data Availability Statement

The datasets generated and supporting the findings of this article are obtainable from the corresponding author upon reasonable request.

References

[1] IEEE, 2020, *International Roadmap for Devices and Systems TM*, IEEE Press, Piscataway, NJ.

[2] Kim, T.-H., Oh, J., Yoo, H., Kim, D., and Torelli, T., 2016, "Criticality of Wafer Edge Inspection and Metrology Data to All-Surface Defectivity Root Cause and Yield Analysis," Proceedings of the Advanced Semiconductor Manufacturing Conference (ASMC'16), Saratoga Springs, NY, May 16–19.

[3] Zhu, J., Liu, J., Xu, T., Yuan, S., Zhang, Z., Jiang, H., Gu, H., Zhou, R., and Liu, S., 2022, "Optical Wafer Defect Inspection at the 10 nm Technology Node and Beyond," Int. J. Extreme Manuf., **4**(3), p. 032001.

[4] Burkeen, F., Vedula, S., and Meeks, S., 2007, "Visualizing the Wafer's Edge," KLA-Tencor Yield Management Solutions Magazine, pp. 18–20.

[5] Morillo, J. D., Houghton, T., Bauer, J. M., Smith, R., and Shay, R., 2005, "Edge and Bevel Automated Defect Inspection for 300 mm Production Wafers in Manufacturing," Proceedings of the IEEE/SEMI Conference and Workshop on Advanced Semiconductor Manufacturing 2005, Munich, Germany, IEEE, pp. 49–52.

[6] Porat, R., Dotan, K., Hemar, S., Levin, L., Li, K., Sung, G., Lin, C.-T., Lin, S.-K., and Wang, H.-I., 2008, "SEM-Based Methodology for Root Cause Analysis of Wafer Edge and Bevel Defects," Proceedings of the 2008 IEEE/SEMI Advanced Semiconductor Manufacturing Conference, Cambridge, MA, IEEE, pp. 11–14.

[7] Altamirano, M., and Skumanich, A., 1998, "Enhanced Defect Detection Capability Using Combined Brightfield/Darkfield Imaging," In-Line Characterization Techniques for Performance and Yield Enhancement in Microelectronic Manufacturing II, Vol. 3509. SPIE, pp. 60–64.

[8] Pan, B., Yang, Y., Bian, J., Hu, X., and Zhang, W., 2019, "Quantum dot Decorated Nano-Pyramid Fiber Tip for Scanning Near-Field Optical Microscopy," Opt. Commun., **445**(15), pp. 273–276.

[9] Bek, A., Vogelgesang, R., and Kern, K., 2006, "Apertureless Scanning Near Field Optical Microscope With Sub-10 nm Resolution," Rev. Sci. Instrum., **77**(4), p. 043703.

[10] Purandare, S., Zhu, J., Zhou, R., Popescu, G., Schwing, A., and Goddard, L. L., 2019, "Optical Inspection of Nanoscale Structures Using a Novel Machine Learning Based Synthetic Image Generation Algorithm," Opt. Express, **27**(13), pp. 17743–17762.

[11] Wang, T., Chen, Y., Qiao, M., and Snoussi, H., 2018, "A Fast and Robust Convolutional Neural Network-Based Defect Detection Model in Product Quality Control," Int. J. Adv. Manuf. Technol., **94**(9–12), pp. 3465–3471.

[12] Chien, J.-C., Wu, M.-T., and Lee, J.-D., 2020, "Inspection and Classification of Semiconductor Wafer Surface Defects Using CNN Deep Learning Networks," Appl. Sci., **10**(15), p. 5340.

[13] Cheon, S., Lee, H., Kim, C. O., and Lee, S. H., 2019, "Convolutional Neural Network for Wafer Surface Defect Classification and the Detection of Unknown Defect Class," IEEE Trans. Semicond. Manuf., **32**(2), pp. 163–170.

[14] Li, Y., Yang, J., Pan, Z., and Tong, W., 2020, "Nanoscale Pore Structure and Mechanical Property Analysis of Coal: An Insight Combining AFM and SEM Images," Fuel, **260**(15), p. 116352.

[15] Madsen, J., Liu, P., Kling, J., Wagner, J. B., Hansen, T. W., Winther, O., and Schiøtz, J., 2018, "A Deep Learning Approach to Identify Local Structures in Atomic-Resolution Transmission Electron Microscopy Images," Adv. Theory Simul., **1**(8), p. 1800037.

[16] Zhang, D., Zhu, Y., Liu, L., Ying, X., Hsiung, C.-E., Sougrat, R., Li, K., and Han, Y., 2018, "Atomic-Resolution Transmission Electron Microscopy of Electron Beam–Sensitive Crystalline Materials," Science, **359**(6376), pp. 675–679.

[17] Iida, S., Nagai, T., and Uchiyama, T., 2019, "Standard Wafer With Programed Defects to Evaluate the Pattern Inspection Tools for 300-mm Wafer Fabrication for 7-nm Node and Beyond," J. Micro/Nanolithogr. MEMS MOEMS, **18**(2), pp. 023505–023505.

[18] Kolenov, D., and Pereira, S. F., 2020, "Machine Learning Techniques Applied for the Detection of Nanoparticles on Surfaces Using Coherent Fourier Scatterometry," Opt. Express, **28**(13), pp. 19163–19186.

[19] Lee, C., Lee, S.-K., and Tarbutton, J. A., 2014, "Novel Design and Sensitivity Analysis of Displacement Measurement System Utilizing Knife Edge Diffraction for Nanopositioning Stages," Rev. Sci. Instrum., **85**(9), p. 095113.

[20] Lee, C., Lee, S.-K., and Tarbutton, J. A., 2015, "Positioning Control Effectiveness of Optical Knife Edge Displacement Sensor-Embedded Monolithic Precision Stage," Sens. Actuators, A, **233**(1), pp. 390–396.
[21] Lee, C., Jeon, S., Stepanick, C. K., Zolfaghari, A., and Tarbutton, J. A., 2017, "Investigation of Optical Knife Edge Sensor for Low-Cost, Large-Range and Dual-Axis Nanopositioning Stages," Measurement, **103**, pp. 157–164.
[22] Zolfaghari, A., Jeon, S., Stepanick, C. K., and Lee, C., 2017, "A Novel Sensor for Two-Degree-of-Freedom Motion Measurement of Linear Nanopositioning Stage Using Knife Edge Displacement Sensing Technique," Rev. Sci. Instrum., **88**(6), p. 065110.
[23] Jeon, S., Stepanick, C. K., Zolfaghari, A. A., and Lee, C., 2017, "Knife-Edge Interferometry for Cutting Tool Wear Monitoring," Precis. Eng., **50**, pp. 354–360.
[24] Jeon, S., Zolfaghari, A., and Lee, C., 2018, "Dicing Wheel Wear Monitoring Technique Utilizing Edge Diffraction Effect," Measurement, **121**(5), pp. 139–143.
[25] Wang, Z., and Lee, C., 2021, "Knife-Edge Interferogram Analysis for Corrosive Wear Propagation at Sharp Edges," Appl. Opt., **60**(5), pp. 1373–1379.
[26] Wang, Z., Chun, H., and Lee, C., 2021, "Enhancement of Knife-Edge Interferometry for Edge Topography Characterization," Rev. Sci. Instrum., **92**(12), p. 125101.
[27] Wang, Z., Lin, P., and Lee, C., 2022, "Preliminary Study of Photomask Pattern Inspection by Beam-Shaped Knife-Edge Interferometry," Precis. Eng., **77**, pp. 104–109.
[28] Lee, C., Mahajan, S. M., Zhao, R., and Jeon, S., 2016, "A Curved Edge Diffraction-Utilized Displacement Sensor for Spindle Metrology," Rev. Sci. Instrum., **87**(7), p. 075113.
[29] Lee, C., Zhao, R., and Jeon, S., 2017, "A Simple Optical System for Miniature Spindle Runout Monitoring," Measurement, **102**, pp. 42–46.
[30] Kim, J., Lee, S., Chun, H., and Lee, C., 2021, "Compact Curved-Edge Displacement Sensor-Embedded Spindle System for Machining Process Monitoring," J. Manuf. Processes, **64**, pp. 1255–1260.
[31] Wang, Z., Lin, P., Nguyen, P., Wang, J., and Lee, C., 2024, "Line-Edge-Roughness Characterization of Photomask Patterns and Lithography-Printed Patterns," Precis. Eng. J., **88**, pp. 235–240.
[32] Lee, C., Zolfaghari, A., Kim, G. H., and Jeon, S., 2019, "An Optical Measurement Technique for Dynamic Stiffness and Damping of Precision Spindle System," Measurement, **131**, pp. 61–68.
[33] Lee, C., 2019, "A First Review of Optical Edge-Diffraction Technology for Precision Dimensional Metrology," Int. J. Adv. Manuf. Technol., **102**(5–8), pp. 2465–2480.
[34] Zhang, Y., and Leithead, W. E., 2007, "Approximate Implementation of the Logarithm of the Matrix Determinant in Gaussian Process Regression," J. Stat. Comput. Simul., **77**(4), pp. 329–348.
[35] Mallat, S., 2012, "Group Invariant Scattering," Commun. Pure Appl. Math., **65**(10), pp. 1331–1398.
[36] Andén, J., and Mallat, S., 2014, "Deep Scattering Spectrum," IEEE Trans. Signal Process., **62**(16), pp. 4114–4128.
[37] Narayan, S. K., Vithin, A. V.S., and Gannavarpu, R., 2023, "Deep Learning Assisted Non-Contact Defect Identification Method Using Diffraction Phase Microscopy," Appl. Opt., **62**(20), pp. 5433–5442.
[38] Pandey, D., Ramaiah, J., Ajithaprasad, S., and Gannavarpu, R., 2022, "Subspace Analysis Based Machine Learning Method for Automated Defect Detection From Fringe Patterns," Optik, **270**, p. 170026.
[39] Vishnoi, A., Madipadaga, A., Ajithaprasad, S., and Gannavarpu, R., 2021, "Automated Defect Identification From Carrier Fringe Patterns Using Wigner–Ville Distribution and a Machine Learning-Based Method," Appl. Opt., **60**(15), pp. 4391–4397.